

STUDY OF THE PROCESS $e^+e^- \rightarrow \pi^+\pi^-$ IN THE ENERGY REGION $400 < \sqrt{s} < 1000$ MeV

*M. N. Achasov**, *K. I. Beloborodov*, *A. V. Berdyugin*, *A. G. Bogdanchikov*, *A. V. Bozhenok*,
A. D. Bukin, *D. A. Bukin*, *T. V. Dimova*, *V. P. Druzhinin*, *V. B. Golubev*, *I. A. Koop*,
A. A. Korol, *S. V. Koshuba*, *A. P. Lysenko*, *A. V. Otboev*, *E. V. Pakhtusova*,
S. I. Serednyakov, *Yu. M. Shatunov*, *V. A. Sidorov*, *Z. K. Silagadze*, *A. N. Skrinsky*,
Yu. A. Tikhonov, *A. V. Vasiljev*

*Budker Institute of Nuclear Physics,
Siberian Branch of the Russian Academy of Sciences
630090, Novosibirsk, Russia*

*Novosibirsk State University
630090, Novosibirsk, Russia*

Submitted 24 June 2005

The cross section of the process $e^+e^- \rightarrow \pi^+\pi^-$ was measured in the spherical neutral detector experiment at the VEPP-2M collider in the energy region $400 < \sqrt{s} < 1000$ MeV. This measurement was based on about $12.4 \cdot 10^6$ selected collinear events, which include $7.4 \cdot 10^6$ $e^+e^- \rightarrow e^+e^-$, $4.5 \cdot 10^6$ $e^+e^- \rightarrow \pi^+\pi^-$, and $0.5 \cdot 10^6$ $e^+e^- \rightarrow \mu^+\mu^-$ selected events. The systematic uncertainty of the cross section determination is 1.3%. The ρ -meson parameters were determined as $m_\rho = 774.9 \pm 0.4 \pm 0.5$ MeV, $\Gamma_\rho = 146.5 \pm 0.8 \pm 1.5$ MeV, and $\sigma(\rho \rightarrow \pi^+\pi^-) = 1220 \pm 7 \pm 16$ nb and the parameters of the G -parity suppressed decay $\omega \rightarrow \pi^+\pi^-$ as $\sigma(\omega \rightarrow \pi^+\pi^-) = 29.9 \pm 1.4 \pm 1.0$ nb and $\phi_{\rho\omega} = 113.5 \pm 1.3 \pm 1.7$ degree.

PACS: 13.66.Bc, 13.66.Jn, 13.25.Jx, 12.40.Vv

1. INTRODUCTION

The cross section of the $e^+e^- \rightarrow \pi^+\pi^-$ process in the energy region $\sqrt{s} < 1000$ MeV can be described within the vector meson dominance model and is determined by the transitions $V \rightarrow \pi^+\pi^-$ of the light vector mesons ($V = \rho, \omega, \rho', \rho''$) into the final state. The main contribution in this energy region comes from the $\rho \rightarrow \pi^+\pi^-$ and from the G -parity violating $\omega \rightarrow \pi^+\pi^-$ transitions. Studies of the $e^+e^- \rightarrow \pi^+\pi^-$ reaction allow determining the ρ and ω meson parameters and provide information on the G -parity violation mechanism.

At low energies, the $e^+e^- \rightarrow \pi^+\pi^-$ cross section gives the dominant contribution to the celebrated ratio

$$R(s) = \frac{\sigma(e^+e^- \rightarrow \text{hadrons})}{\sigma(e^+e^- \rightarrow \mu^+\mu^-)},$$

*E-mail: achasov@inp.nsk.su

which is used for calculation of the dispersion integrals (for example, for evaluation of the electromagnetic running coupling constant at the Z -boson mass $\alpha_{em}(s = m_Z^2)$) or for determination of the hadronic contribution a_μ^{hadr} to the anomalous magnetic moment of the muon, which is nowadays measured with very high accuracy $5 \cdot 10^{-6}$ [1, 2].

Assuming conservation of the vector current (CVC) in the isospin symmetry limit, the spectral function of the $\tau^\pm \rightarrow \pi^\pm \pi^0 \nu_\tau$ decay can be related to the isovector part of the $e^+e^- \rightarrow \pi^+\pi^-$ cross section. The spectral function was determined with high precision in Refs. [3–5]. The comparison of the $e^+e^- \rightarrow \pi^+\pi^-$ cross section with what follows from the spectral function provides an accurate test of the CVC hypothesis.

The process $e^+e^- \rightarrow \pi^+\pi^-$ in the energy region $\sqrt{s} < 1000$ MeV was studied in several experiments [6–19] during more than 30 years. In the present work, the results of the $e^+e^- \rightarrow \pi^+\pi^-$ cross section

measurement with spherical neutral detector (SND) at $390 \leq \sqrt{s} \leq 980$ MeV are reported.

2. EXPERIMENT

The SND [20] operated from 1995 to 2000 at the VEPP-2M [21] collider in the energy range \sqrt{s} from 360 to 1400 MeV. The detector contains several sub-systems. The tracking system includes two cylindrical drift chambers. The three-layer spherical electromagnetic calorimeter is based on NaI(Tl) crystals. The muon/veto system consists of plastic scintillation counters and two layers of streamer tubes. The calorimeter energy and angular resolutions depend on the photon energy as

$$(\sigma_E/E) \% = 4.2 \% / \sqrt[4]{E[\text{GeV}]}$$

and

$$\sigma_{\phi, \theta} = 0.82^\circ / \sqrt{E[\text{GeV}]} \oplus 0.63^\circ.$$

The tracking system angular resolution is about 0.5° and 2° for azimuthal and polar angles respectively.

In 1996–2000 the SND collected data in the energy region $\sqrt{s} < 980$ MeV with the integrated luminosity about 10.0 pb^{-1} . The beam energy was calculated from the magnetic field value in the bending magnets of the collider. The accuracy of the energy setting is about 0.1 MeV. The beam energy spread varies in the range from 0.06 MeV at $\sqrt{s} = 360$ MeV to 0.35 MeV at $\sqrt{s} = 970$ MeV.

3. DATA ANALYSIS

The cross section of the $e^+e^- \rightarrow \pi^+\pi^-$ process was measured as follows.

1. The collinear events $e^+e^- \rightarrow e^+e^-, \pi^+\pi^-, \mu^+\mu^-$ were selected.
2. The selected events were sorted into the two classes: e^+e^- and $\pi^+\pi^-, \mu^+\mu^-$ using the energy deposition in the calorimeter layers.
3. The $e^+e^- \rightarrow e^+e^-$ events were used for integrated luminosity determination. The events of the $e^+e^- \rightarrow \mu^+\mu^-$ process were subtracted according to the theoretical cross section, integrated luminosity, and detection efficiency.
4. To determine the cross section of the $e^+e^- \rightarrow \pi^+\pi^-$ process, the number of $e^+e^- \rightarrow \pi^+\pi^-$ events in each energy point were normalized to the integrated luminosity and divided by the detection efficiency and radiative correction.

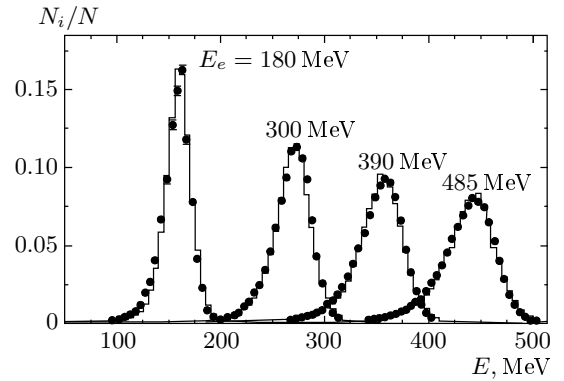


Fig. 1. Energy deposition spectra for electrons with the energies 180, 300, 390, and 485 MeV in experiment (dots) and MC simulation (histogram)

The detection efficiency was obtained from Monte Carlo (MC) simulation [20]. The MC simulation of SND is based on the UNIMOD [22] package. The SND geometrical model description comprises about 10000 distinct volumes and includes details of the SND design. The primary generated particles are tracked through the detector media with the following effects taken into account: ionization losses, multiple scattering, bremsstrahlung of electrons and positrons, Compton effect and Rayleigh scattering, e^+e^- pair production by photons, photoeffect, unstable particles decays, interaction of stopped particles, and nuclear interaction of hadrons [23–25]. After that, the signals produced in each detector element are simulated. The electronics noise, signals pile up, the actual time and amplitude resolutions of the electronics channels and broken channels were taken into account during processing the Monte Carlo events to provide the adaptable account of variable experimental conditions.

The Monte Carlo simulation of the processes $e^+e^- \rightarrow e^+e^-, \mu^+\mu^-, \pi^+\pi^-$ was based on the formula obtained in the Refs. [26–28]. The simulation of the process $e^+e^- \rightarrow e^+e^-$ was performed with the cut $30^\circ < \theta_{e^\pm} < 150^\circ$ on the polar angles of the final electron and positron.

The $e^+e^- \rightarrow e^+e^-, \mu^+\mu^-$ and $\pi^+\pi^-$ events differ by energy deposition in the calorimeter. In the $e^+e^- \rightarrow e^+e^-$ events, the electrons produce an electromagnetic shower with the most probable energy losses about 0.92 of the initial particle energy. The distributions of the energy deposition of the electrons with different energies are shown in Fig. 1. The experimental and simulated spectra are in good agreement. Muons lose their energy by ionization of the calorimeter ma-

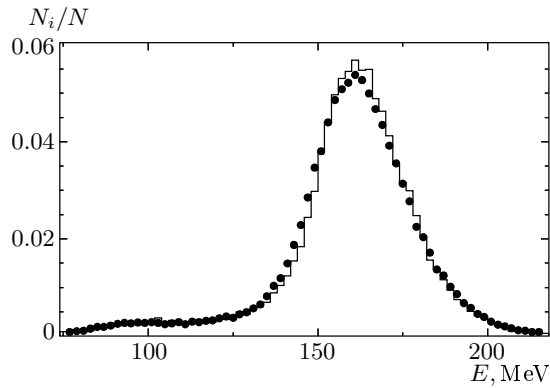


Fig. 2. Energy deposition spectra for the 500 MeV muons in experiment (dots) and MC simulation (histogram)

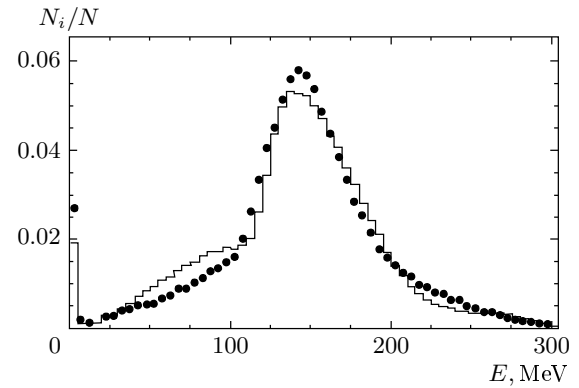


Fig. 4. Energy deposition spectra of the pions with the energy $E_\pi = 300$ MeV. Dots — experiment, histogram — MC simulation

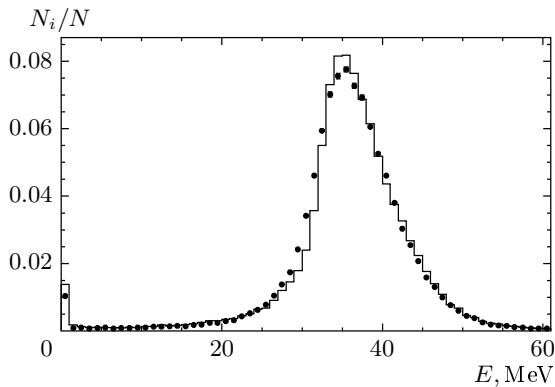


Fig. 3. Spectra of the ionization losses of the pions with the energy $E_\pi > 360$ MeV in the first calorimeter layer. Dots — experiment, histogram — MC simulation

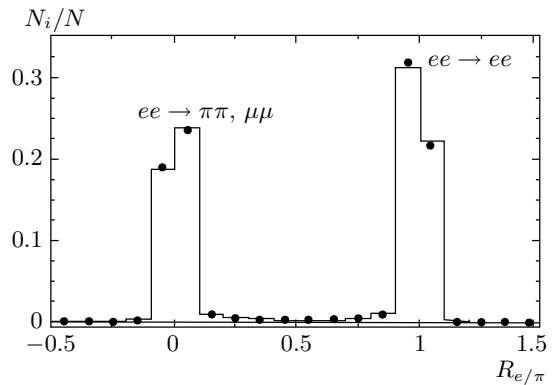


Fig. 5. The e/π discrimination parameter distribution for all collinear events in the energy region \sqrt{s} from 880 to 630 MeV. Dots — experiment, histogram — MC simulation

terial through which they pass and their energy deposition spectra are well modeled in simulation (Fig. 2). The similar ionization losses are experienced by charged pions, and this part of the charged pion energy deposition is well described by simulation (Fig. 3). But pions also lose their energy due to nuclear interactions, which is not so accurately reproduced in simulation. This leads to some difference in the energy deposition spectra in experiment and simulation for charged pions (Fig. 4).

The discrimination between electrons and pions in the SND is based on the difference in the longitudinal energy deposition profiles (deposition in calorimeter layers) for these particles. To fully use the correlations between energy depositions in the calorimeter layers, the corresponding separation parameter was based

on the neural network approach [29]. For each energy point, the neural network — multilayer perceptron was constructed. The network had the input layer consisting of 7 neurons, two hidden layers with 20 neurons each, and the output layer with one neuron. As the input data, the network used the energy depositions of particles in calorimeter layers and the polar angle of one of the particles. The output signal $R_{e/\pi}$ is a number in the interval from -0.5 to 1.5 . The network was trained by using simulated $e^+e^- \rightarrow \pi^+\pi^-$ and $e^+e^- \rightarrow e^+e^-$ events. The distribution of the discrimination parameter $R_{e/\pi}$ is shown in Fig. 5. The $e^+e^- \rightarrow e^+e^-$ events are located in the region $R_{e/\pi} > 0.5$, and the $e^+e^- \rightarrow \pi^+\pi^-, \mu^+\mu^-$ events at $R_{e/\pi} < 0.5$.

3.1. Selection criteria

During the experimental runs, the first-level trigger [20] selects events with one or more tracks in the tracking system and with two clusters in the calorimeter with the spatial angle between the clusters more than 100° . The threshold on energy deposition in a cluster was equal to 25 MeV. The threshold on the total energy deposition in the calorimeter was set equal to 140 MeV in the energy region $\sqrt{s} \geq 850$ MeV, and to 100 MeV, or was absent at all, below 850 MeV. During processing of the experimental data, event reconstruction is performed [20, 30]. For further analysis, events containing two charged particles with $|z| < 10$ cm and $r < 1$ cm were selected. Here, z is the coordinate of the charged particle production point along the beam axis (the longitudinal size of the interaction region depends on the beam energy and varies from 1.5 to 2.5 cm) and r is the distance between the charged particle track and the beam axis in the $r\phi$ plane. The polar angles of the charged particles were bounded by the criterion $55^\circ < \theta < 125^\circ$ and the energy deposition of each of them was required to be greater than 50 MeV. The following cuts on the acollinearity angles in the azimuthal and polar planes were applied: $|\Delta\phi| < 10^\circ$ and $|\Delta\theta| < 10^\circ$. In the event sample selected under these conditions, one has the $e^+e^- \rightarrow e^+e^-$, $\pi^+\pi^-$, $\mu^+\mu^-$ events, cosmic muons background, and a small contribution from the $e^+e^- \rightarrow \pi^+\pi^-\pi^0$ reaction at $\sqrt{s} \approx m_\omega$. The muon system veto was used for suppression of the cosmic muon background (veto = 0).

3.2. The background from cosmic muons and from the $e^+e^- \rightarrow \pi^+\pi^-\pi^0$ process

The number of background events from the $e^+e^- \rightarrow \pi^+\pi^-\pi^0$ process was estimated as

$$N_{3\pi}(s) = \sigma_{3\pi}(s)\epsilon_{3\pi}(s)IL(s), \quad (1)$$

where $\sigma_{3\pi}(s)$ is the cross section of the $e^+e^- \rightarrow \pi^+\pi^-\pi^0$ process with the radiative corrections taken into account, $IL(s)$ is the integrated luminosity, and $\epsilon_{3\pi}(s)$ is the detection probability for the background process obtained from the simulation under the selection criteria described above. The values of $\sigma_{3\pi}(s)$ were taken from the SND measurements [31]. Although $\sigma_{3\pi}(m_\omega) \approx 1300$ nb, the $e^+e^- \rightarrow 3\pi$ process contribution to the total number of collinear events at the ω resonance peak is less than 0.3%. The leading role in the suppression of this background was played by the cuts on the acollinearity angles $\Delta\theta$ and $\Delta\phi$. In order to check the estimate

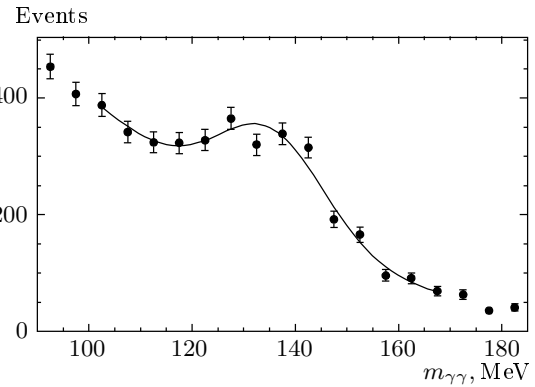


Fig. 6. Two-photon invariant mass $m_{\gamma\gamma}$ distribution at $\sqrt{s} \approx m_\omega$

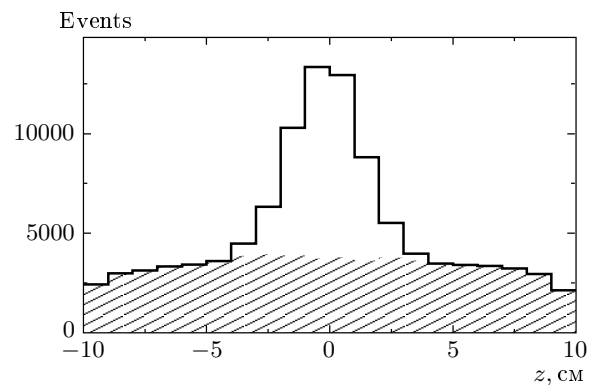


Fig. 7. Distribution of the z coordinate of the charged particle production point along the beam axis for collinear events at $\sqrt{s} = 180$ MeV. Histogram — all events, dashed distribution — events with muon system veto (veto = 1)

in (1), the events containing two and more photons with energy depositions more than 200 MeV were considered.

Because our selection criteria select the $e^+e^- \rightarrow 3\pi$ events with collinear charged pions and therefore the neutral pion in this events has relatively low energy, the constraint on the photon energy deposition greatly suppresses the events other than $e^+e^- \rightarrow 3\pi$ events. To obtain the $e^+e^- \rightarrow 3\pi$ event number $n_{3\pi}$, the invariant mass spectrum $m_{\gamma\gamma}$ (Fig. 6) was fitted by the sum of a Gaussian function and a second-order polynomial:

$$G(m_{\gamma\gamma})n_{3\pi} + P_2(m_{\gamma\gamma})(n - n_{3\pi}).$$

The value of $n_{3\pi}$ agrees with events number calculated according to (1).

The cosmic muon background was suppressed by

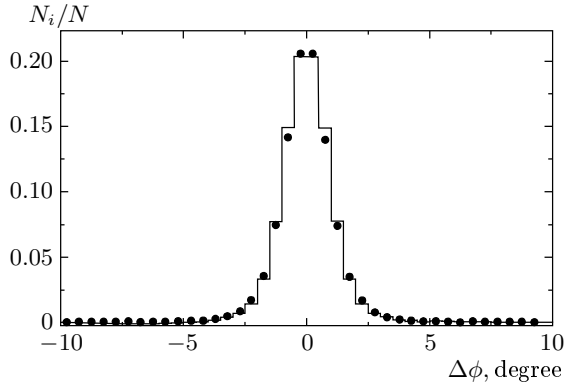


Fig. 8. The $\Delta\phi$ distribution of the $e^+e^- \rightarrow e^+e^-$ events. Dots — experiment, histogram — MC simulation

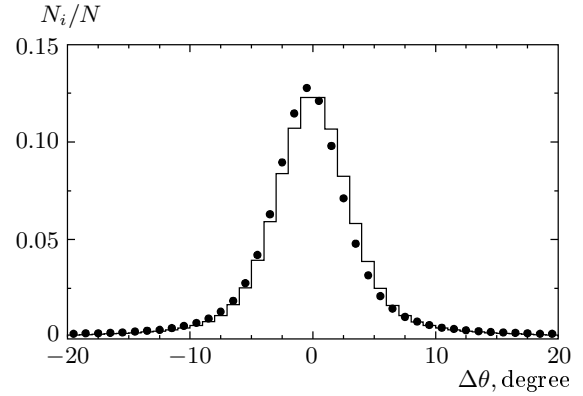


Fig. 11. The $\Delta\theta$ distribution of the $e^+e^- \rightarrow \pi^+\pi^-$ events. Dots — experiment, histogram — MC simulation

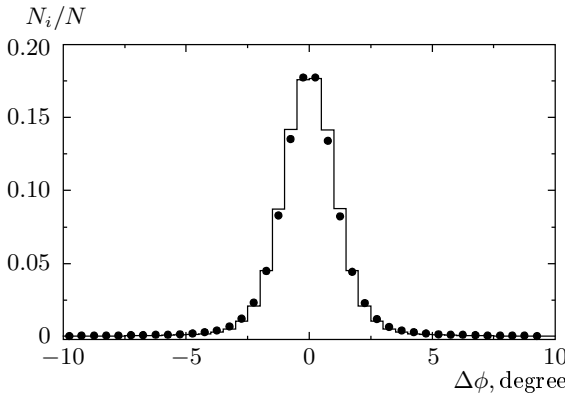


Fig. 9. The $\Delta\phi$ distribution of the $e^+e^- \rightarrow \pi^+\pi^-$ events. Dots — experiment, histogram — MC simulation

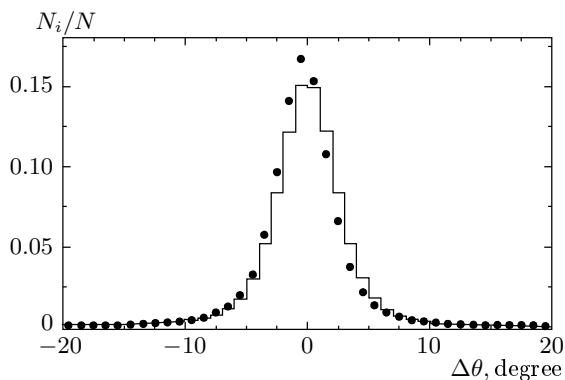


Fig. 10. The $\Delta\theta$ distribution of the $e^+e^- \rightarrow e^+e^-$ events. Dots — experiment, histogram — MC simulation

the muon/veto system. The z coordinate distribution for the charged particle production point along the beam axis is shown in Fig. 7 for collinear events. The e^+e^- annihilation events have the Gaussian distribution peaked at $z = 0$, while the cosmic background distribution is nearly uniform and clearly extends outside the peak. As Fig. 7 shows, the muon system veto (veto = 1) separates cosmic muons from the e^+e^- annihilation events. The residual event number of the cosmic muon background was estimated from the formula

$$N_\mu = \nu_\mu T, \tag{2}$$

where $\nu_\mu \approx 1.3 \cdot 10^{-3}$ Hz is the frequency of cosmic background registration under the applied selection criteria and T is the time of data taking. The value of ν_μ was obtained by using data collected in special runs without beams in the collider. The first-level trigger counting rate in these runs was 2 Hz. The contribution of the cosmic background to the total number of selected collinear events depends on the energy \sqrt{s} and varies from 0.1 to 1 %.

The $e^+e^- \rightarrow \pi^+\pi^-\pi^0$ events are concentrated in the $R_{e/\pi}$ discrimination parameter region $R_{e/\pi} < 0.5$. The cosmic background events at the energies $\sqrt{s} > 600$ MeV also fall in the area $R_{e/\pi} < 0.5$, because the energy deposition of the cosmic muons is much lower than the energy deposition in the $e^+e^- \rightarrow e^+e^-$ events. For lower center-of-mass energies, the cosmic background moves to the area $R_{e/\pi} > 0.5$, because the energy depositions are close in this case.

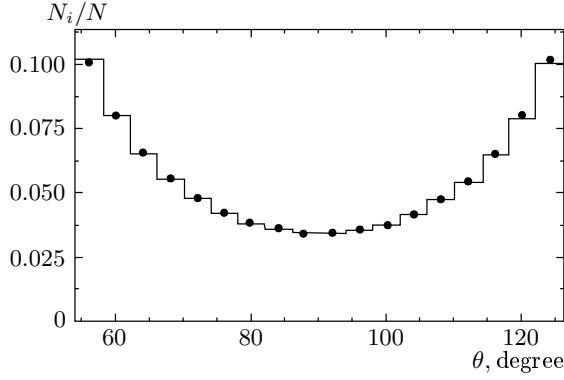


Fig. 12. The θ angle distribution of the $e^+e^- \rightarrow e^+e^-$ events. Dots — experiment, histogram — MC simulation

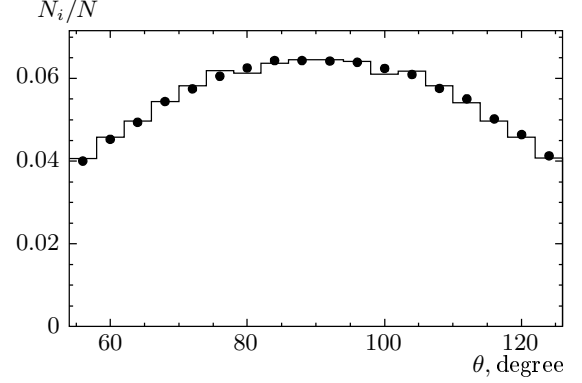


Fig. 13. The θ angle distribution of the $e^+e^- \rightarrow \pi^+\pi^-$ events. Dots — experiment, histogram — MC simulation

3.3. Detection efficiency

The $\Delta\phi$ and $\Delta\theta$ distributions of the $e^+e^- \rightarrow e^+e^-$ and $e^+e^- \rightarrow \pi^+\pi^-$ events are shown in Figs. 8, 9, 10, and 11. Experiment and simulation agree rather well. As a measure of the systematic uncertainty due to the $\Delta\theta$ cut, the following value was used:

$$\delta_{\Delta\theta} = \frac{\delta_{\Delta\theta}^{\pi\pi}}{\delta_{\Delta\theta}^{ee}}, \quad (3)$$

where

$$\delta_{\Delta\theta}^x = \frac{n_x(|\Delta\theta| < 10^\circ)}{N_x(|\Delta\theta| < 20^\circ)} \bigg/ \frac{m_x(|\Delta\theta| < 10^\circ)}{M_x(|\Delta\theta| < 20^\circ)}, \quad x = \pi\pi(ee).$$

Here, $n_x(|\Delta\theta| < 10^\circ)$ and $m_x(|\Delta\theta| < 10^\circ)$ are the numbers of experimental and simulated events, selected under the condition $|\Delta\theta| < 10^\circ$, while $N_x(|\Delta\theta| < 20^\circ)$ and $M_x(|\Delta\theta| < 20^\circ)$ are the numbers of experimental and simulated events with $|\Delta\theta| < 20^\circ$. The $\delta_{\Delta\theta}$ does not depend on energy, its average value is equal to 0.999, and it has the systematic spread 0.4%. This systematic spread was added to the error of the cross section measurement at each energy point. The systematic error due to the $\Delta\phi$ cut is significantly lower and was neglected.

The polar angle distributions for the $e^+e^- \rightarrow e^+e^-$ and $e^+e^- \rightarrow \pi^+\pi^-$ processes are shown in Figs. 12 and 13. The ratio of these θ distributions is shown in Fig. 14. The experimental and simulated distributions are in agreement. To estimate the systematic inaccuracy due to the θ angle selection cut, the following ratio was used:

$$\delta_\theta = \frac{\delta(\theta_x)}{\delta(55^\circ)}, \quad (4)$$

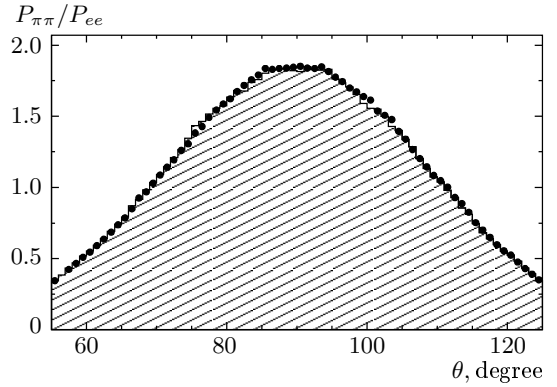


Fig. 14. The ratio of θ distributions of the $e^+e^- \rightarrow \pi^+\pi^-$ and $e^+e^- \rightarrow e^+e^-$ processes. Dots — experiment, histogram — MC simulation

where

$$\delta(\theta_x) = \frac{N_{\pi\pi}(\theta_x < \theta < 180^\circ - \theta_x)}{N_{ee}(\theta_x < \theta < 180^\circ - \theta_x)} \bigg/ \frac{M_{\pi\pi}(\theta_x < \theta < 180^\circ - \theta_x)}{M_{ee}(\theta_x < \theta < 180^\circ - \theta_x)}, \quad 50^\circ < \theta_x < 90^\circ.$$

Here, $N_{\pi\pi}(\theta_x < \theta < 180^\circ - \theta_x)$, $N_{ee}(\theta_x < \theta < 180^\circ - \theta_x)$, $M_{\pi\pi}(\theta_x < \theta < 180^\circ - \theta_x)$, and $M_{ee}(\theta_x < \theta < 180^\circ - \theta_x)$ are the experimental and simulated $e^+e^- \rightarrow \pi^+\pi^-$ and $e^+e^- \rightarrow e^+e^-$ event numbers in the angular range $\theta_x < \theta < 180^\circ - \theta_x$. The maximal difference of δ_θ from unity was found to be 0.8%. This value was taken as a systematic error $\sigma_\theta = 0.8\%$ associated with the angular selection cut.

In the tracking system, the particle track can be lost due to reconstruction inefficiency. The probabili-

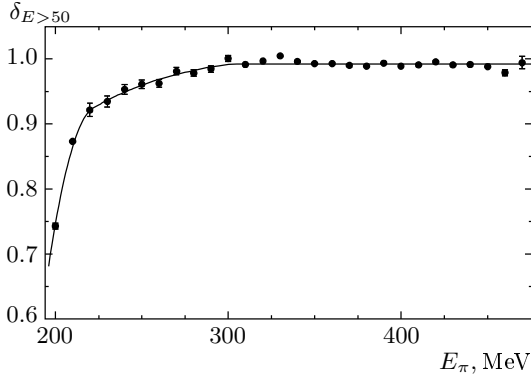


Fig. 15. The $\delta_{E>50}$ correction coefficient associated with the pion energy deposition cut vs the pion energy E_π

ties to find the track was determined by using experimental data themselves. It was found to be $\varepsilon_e \approx 0.996$ for electrons and $\varepsilon_\pi \approx 0.995$ for pions. In simulation, these values do not actually differ from unity, while in reality, the track finding probability for electrons is slightly greater than for pions. Therefore, the detection efficiency was multiplied by the correction coefficient

$$\delta_{rec} = \left(\frac{\varepsilon_\pi}{\varepsilon_e} \right)^2 = 0.997. \quad (5)$$

Pions can be lost due to the nuclear interaction in the detector material before the tracking system, for example, via the reaction $\pi^\pm N \rightarrow \pi^\pm N$ with the final pion scattered at a large angle or via the charge exchange reaction $\pi^\pm N \rightarrow \pi^0 N$. As a measure of systematic inaccuracy associated with this effect, the difference from unity of the following quantity was used:

$$\delta_{nucl} = \left(\frac{1 - \frac{n}{3N}}{1 - \frac{m}{3M}} \right)^2. \quad (6)$$

Here, N and M are the pion numbers in experiment and simulation; n and m are the pion numbers in experiment and simulation in the case where a track in the drift chamber nearest to the beam pipe was detected but the corresponding track in the second drift chamber and associated cluster in the calorimeter was not found. The particle loss probability was divided by 3, the ratio of the amounts of matter between the drift chambers and before the tracking system. The deviation of δ_{nucl} from 1 was taken as a systematic error $\sigma_{nucl} = 0.2\%$.

Uncertainties in simulation of pion nuclear interactions imply that the cut on the particle energy deposition leads to an inaccuracy in the detection efficiency

of the $e^+e^- \rightarrow \pi^+\pi^-$ process. To take this inaccuracy into account, the detection efficiency was multiplied by the correction coefficients. The correction coefficients were obtained by using events of the $e^+e^- \rightarrow \pi^+\pi^-\pi^0$ reaction [30–32]. Pion energies in the $e^+e^- \rightarrow \pi^+\pi^-\pi^0$ events were determined via the kinematic fit. The pion energies were divided into the 10 MeV wide bins. For each bin, the correction coefficient (Fig. 15) was obtained as

$$\delta_{E>50} = \left[\frac{n_i/N_i}{m_i/M_i} \right]^2, \quad (7)$$

where i is the bin number, N_i and M_i are the pion numbers in experiment and simulation selected in the i th bin by the kinematic fit without any cut on the energy deposition in the calorimeter; and n_i and m_i are the pion numbers in experiment and simulation under the condition that the pion energy deposition is greater than 50 MeV. To estimate systematic errors in determining these correction coefficients, we considered the ratio of the probability that both pions in simulated $e^+e^- \rightarrow \pi^+\pi^-$ events have energy deposition more than 50 MeV to the quantity $(m_i/M_i)^2$. This ratio is 0.994 at $\sqrt{s} > 420$ MeV and about 0.97 at $\sqrt{s} < 420$ MeV. The difference of this ratio from unity was taken as a systematic error $\sigma_{E>50}$ of the $\delta_{E>50}$ correction coefficient determination: $\sigma_{E>50} = 0.6\%$ at $\sqrt{s} > 420$ MeV and $\sigma_{E>50} = 3\%$ at $\sqrt{s} < 420$ MeV.

In the energy region $\sqrt{s} = 840\text{--}970$ MeV, the probability to hit the muon/veto system for muons and pions varies from 1% to 93%, and from 0.5% to 3% respectively. The usage of the muon system veto for event selection (veto = 0) leads to inaccuracy in the measured cross section determination due to the uncertainty in the simulation of the muons and pions traversing the detector at $\sqrt{s} > 840$ MeV. To obtain the necessary corrections, the events close to the median plane $\phi < 10^\circ$, $170^\circ < \phi < 190^\circ$, $\phi > 350^\circ$, where the cosmic background is minimal, were used. The $e^+e^- \rightarrow \pi^+\pi^-$ cross section was measured with (veto = 0) and without (veto \geq 0) using the muon system, and the following correction coefficient was obtained for each energy point:

$$\delta_{veto} = \frac{\sigma(e^+e^- \rightarrow \pi^+\pi^-; \text{veto} \geq 0)}{\sigma(e^+e^- \rightarrow \pi^+\pi^-; \text{veto} = 0)}. \quad (8)$$

It was found that $\delta_{veto} = 0.95$ at $\sqrt{s} = 970$ MeV and quickly rises up to 1 for lower energies.

The detection efficiencies of the processes $e^+e^- \rightarrow \pi^+\pi^-$, $\mu^+\mu^-$ and e^+e^- after all the applied corrections are shown in Fig. 16. The detection efficiency is independent of energy for the $e^+e^- \rightarrow e^+e^-$

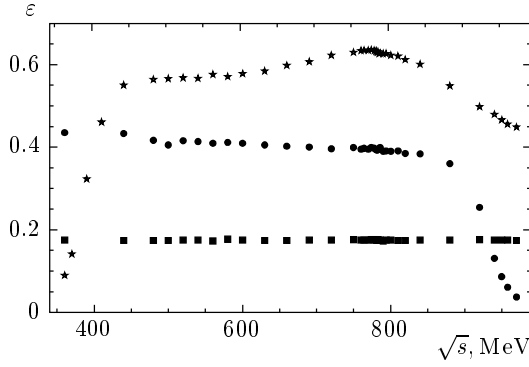


Fig. 16. The detection efficiencies $\varepsilon_{\pi\pi}$ (\star), ε_{ee} (\blacksquare), and $\varepsilon_{\mu\mu}$ (\bullet), of the $e^+e^- \rightarrow \pi^+\pi^-$, $\mu^+\mu^-$ and e^+e^- processes

reaction but depends on it for the $e^+e^- \rightarrow \mu^+\mu^-$ and $\pi^+\pi^-$ processes. The decrease of the $e^+e^- \rightarrow \mu^+\mu^-$ process detection efficiency at $\sqrt{s} > 800$ MeV is caused by the fact that the probability for muons to hit the muon system rises with energy. The detection efficiency of the $e^+e^- \rightarrow \pi^+\pi^-$ process at $\sqrt{s} > 500$ MeV is determined mainly by the cuts on the pion angles. Below 500 MeV, the detection efficiency decreases due to the cut on the pion energy deposition in the calorimeter. The statistical error $\leq 1\%$ of the detection efficiency determination was added to the cross section measurement error at each energy point. The total systematic error of the detection efficiency determination $\sigma_{eff} = \sigma_{E>50} \oplus \sigma_{nucl} \oplus \sigma_{\theta}$ is $\sigma_{eff} = 1\%$ at $\sqrt{s} \geq 420$ MeV and $\sigma_{eff} = 3.1\%$ at $\sqrt{s} < 420$ MeV.

3.4. Measurement of the $e^+e^- \rightarrow \pi^+\pi^-$ cross section

The number of selected events in the regions $R_{e/\pi} < 0.5$ and $R_{e/\pi} > 0.5$ are

$$N = N_{\pi\pi} + N_{ee} + N_{\mu\mu} + N_{\mu} + N_{3\pi}, \quad (9)$$

$$M = M_{\pi\pi} + M_{ee} + M_{\mu\mu} + M_{\mu} + M_{3\pi}. \quad (10)$$

Here, N and M are the event numbers in the respective regions $R_{e/\pi} < 0.5$ and $R_{e/\pi} > 0.5$. N_{μ} , M_{μ} and $N_{3\pi}$, $M_{3\pi}$ are the numbers of background events due to cosmic muons and the $e^+e^- \rightarrow \pi^+\pi^-\pi^0$ process, calculated as described above. The $e^+e^- \rightarrow \mu^+\mu^-$ process event number can be written as

$$N_{\mu\mu} = \sigma_{\mu\mu}\varepsilon_{\mu\mu}(1 - \epsilon_{\mu\mu})IL, \quad (11)$$

$$M_{\mu\mu} = \sigma_{\mu\mu}\varepsilon_{\mu\mu}\epsilon_{\mu\mu}IL, \quad (12)$$

where $\sigma_{\mu\mu}$ is the $e^+e^- \rightarrow \mu^+\mu^-$ process cross section obtained according to Ref. [27], $\varepsilon_{\mu\mu}$ is the process detection efficiency, $\epsilon_{\mu\mu}$ is the probability for the $e^+e^- \rightarrow \mu^+\mu^-$ process events to have $R_{e/\pi} > 0.5$, and IL is the integrated luminosity,

$$IL = \frac{M_{ee}}{\sigma_{ee}\varepsilon_{ee}\epsilon_{ee}}, \quad (13)$$

where ε_{ee} and ϵ_{ee} are the detection efficiency and the probability to have $R_{e/\pi} > 0.5$ for the process $e^+e^- \rightarrow e^+e^-$, and σ_{ee} is the process cross section with the $30^\circ < \theta < 150^\circ$ angular cut for the electron and positron in the final state. The cross section σ_{ee} was calculated using the BHWIDE 1.04 [33] code with the accuracy 0.5%. The $e^+e^- \rightarrow \pi^+\pi^-$ process event number with $R_{e/\pi} > 0.5$ and the $e^+e^- \rightarrow e^+e^-$ process event number with $R_{e/\pi} < 0.5$ can be written as

$$N_{ee} = \frac{1 - \epsilon_{ee}}{\epsilon_{ee}} M_{ee} = \lambda_{ee} M_{ee},$$

$$M_{\pi\pi} = \frac{1 - \epsilon_{ee}}{\epsilon_{ee}} N_{\pi\pi} = \lambda_{\pi\pi} N_{\pi\pi}.$$

The $e^+e^- \rightarrow e^+e^-$ process event number with $R_{e/\pi} > 0.5$ and the $e^+e^- \rightarrow \pi^+\pi^-$ process event number with $R_{e/\pi} < 0.5$ are equal to

$$M_{ee} = \frac{M - M_{\mu} - \lambda_{\pi\pi}(N - N_{\mu})}{\kappa - \Delta\lambda_{\pi\pi}}, \quad (14)$$

$$N_{\pi\pi} = N - N_{\mu} - M_{ee}\Delta, \quad (15)$$

where

$$\Delta = \lambda_{ee} + \frac{\sigma_{\mu\mu}\varepsilon_{\mu\mu}(1 - \epsilon_{\mu\mu}) + N_{3\pi}/IL}{\sigma_{ee}\varepsilon_{ee}\epsilon_{ee}},$$

$$\kappa = 1 + \frac{\sigma_{\mu\mu}\varepsilon_{\mu\mu}\epsilon_{\mu\mu} + M_{3\pi}/IL}{\sigma_{ee}\varepsilon_{ee}\epsilon_{ee}}.$$

The percentage of each process in the selected events versus the energy \sqrt{s} is shown in Fig. 17. The experimental angular distributions agree with the sum of distributions for each process weighted according to its contribution (Fig. 18).

The $e^+e^- \rightarrow \pi^+\pi^-$ process cross section is calculated from the formula

$$\begin{aligned} \sigma_{\pi\pi} &= \frac{N_{\pi\pi}}{IL\varepsilon_{\pi\pi}(1 - \epsilon_{\pi\pi})} = \\ &= \frac{\sigma_{ee}\varepsilon_{ee}\epsilon_{ee}}{\varepsilon_{\pi\pi}(1 - \epsilon_{\pi\pi})} \left(\frac{\kappa - \Delta\lambda_{\pi\pi}}{M - M_{\mu} - \lambda_{\pi\pi}N} - \Delta \right). \end{aligned} \quad (16)$$

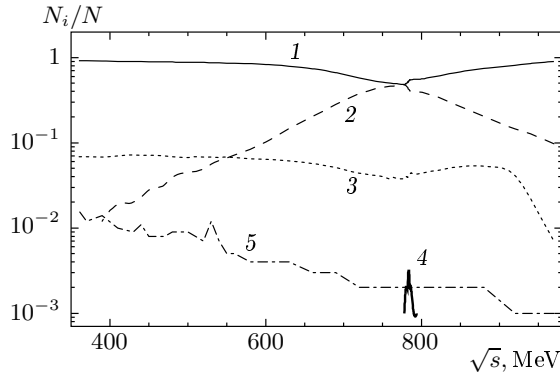


Fig. 17. The percentage of the $e^+e^- \rightarrow e^+e^-$ (1), $\pi^+\pi^-$ (2), $\mu^+\mu^-$ (3), $\pi^+\pi^-\pi^0$ (4) and cosmic background (5) vs the energy \sqrt{s}

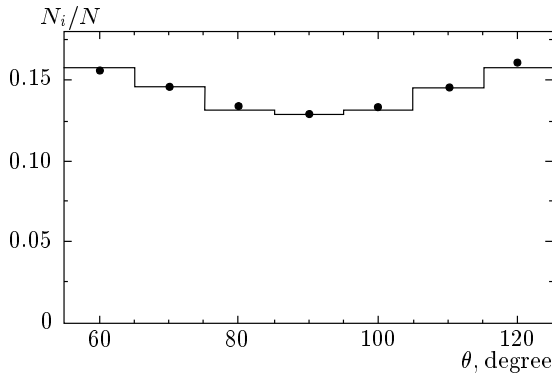


Fig. 18. The θ angle distributions of all collinear events at \sqrt{s} from 880 MeV to 630 MeV. Dots — experiment, histogram — MC simulation

To estimate the systematic uncertainty due to $e-\pi$ discrimination, the pseudo $\pi\pi$ and pseudo ee events in the experiment and simulation were formed. The pseudo $\pi\pi$ events were constructed by using pions from the $e^+e^- \rightarrow \pi^+\pi^-\pi^0$ reaction. To construct the pseudo $\pi\pi$ event with the pions having energy E_0 , two charged pions with energies E_π such that $|E_0 - E_\pi| < 10$ MeV were used from two separate $e^+e^- \rightarrow \pi^+\pi^-\pi^0$ events. Of course, such pseudo $\pi\pi$ events are in general not collinear, but this is irrelevant for our purposes here. The pseudo ee event was constructed analogously from the particles of two separate collinear events such that their partners in these events have energy depositions in the calorimeter layers typical for electrons. Figures 19 and 20 show the probabilities for the discrimination parameter to have values less than some magnitude in experiment and simulation for such pseudo events. Using these distributions, the corrections to the probabilities

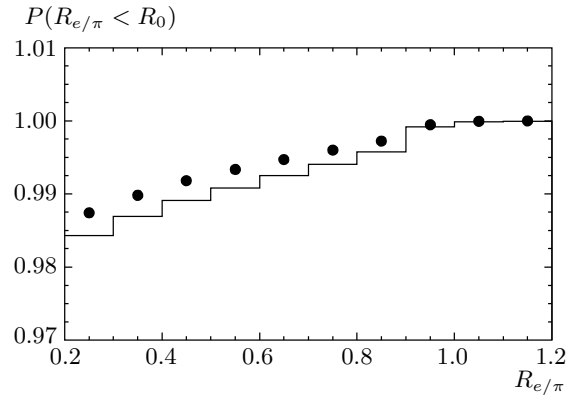


Fig. 19. The probability of the pseudo $\pi\pi$ events to have the $R_{e/\pi}$ value less than some R_0 . Dots — experiment, histogram — MC simulation

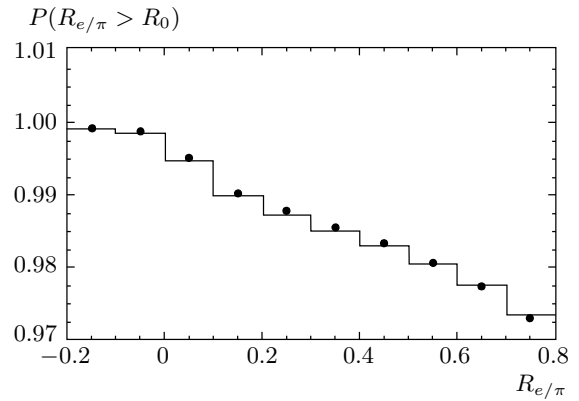


Fig. 20. The probability of the pseudo ee events to have the $R_{e/\pi}$ value greater than some R_0 . Dots — experiment, histogram — MC simulation

for the separation parameter $R_{e/\pi}$ to be greater or less than 0.5 was obtained. The difference between cross sections measured with and without these corrections was taken as a systematic error and its value does not exceed 0.5 % for different energy points.

The obtained cross sections together with the radiative corrections δ_{rad} , including the initial and final state radiation, are presented in Table 1. The δ_{rad} radiative correction was calculated according to Ref. [28]. The accuracy of its determination is 0.2 %. Given the radiative corrections, the Born cross section for the $e^+e^- \rightarrow \pi^+\pi^-$ process can be obtained as

$$\sigma_0(s) = \frac{\sigma_{\pi\pi}(s)}{\delta_{rad}(s)}. \quad (17)$$

The value of $\delta_{rad}(s)$ depends on the cross section at

Table 1. The results of the $e^+e^- \rightarrow \pi^+\pi^-$ cross section measurements. $\sigma_{\pi\pi}$ is the $e^+e^- \rightarrow \pi^+\pi^-$ cross section with the radiative corrections due to the initial and final state radiation taken into account, δ_{rad} is the radiative correction due to the initial and final state radiation, σ_0 and $|F_\pi|^2$ are the cross section and the form factor of the $e^+e^- \rightarrow \pi^+\pi^-$ process after the radiative corrections were undressed, and $\sigma_{\pi\pi}^{pol}$ is the $e^+e^- \rightarrow \pi^+\pi^-$ undressed cross section without vacuum polarization but with the final state radiation. Only uncorrelated errors are shown. The correlated systematic error σ_{sys} is 1.3 % for $\sqrt{s} \geq 420$ MeV and 3.2 % for $\sqrt{s} < 420$ MeV

\sqrt{s} , MeV	$\sigma_{\pi\pi}$, nb	δ_{rad}	σ_0 , nb	$ F_\pi ^2$	$\sigma_{\pi\pi}^{pol}$, nb
970.0	118.12± 2.76	1.491	79.20± 1.85	3.91± 0.09	77.53± 1.81
958.0	137.16± 2.94	1.454	94.34± 2.02	4.56± 0.10	92.16± 1.97
950.0	150.02± 2.85	1.430	104.88± 1.99	4.99± 0.09	102.35± 1.94
940.0	166.55± 2.27	1.400	119.00± 1.62	5.56± 0.08	116.01± 1.58
920.0	204.99± 7.14	1.340	152.96± 5.33	6.89± 0.24	148.60± 5.18
880.0	310.82± 3.52	1.220	254.67± 2.88	10.65± 0.12	245.94± 2.78
840.0	513.80± 4.76	1.106	464.48± 4.30	17.99± 0.17	446.64± 4.13
820.0	676.03± 5.99	1.055	640.60± 5.68	23.86± 0.21	614.57± 5.45
810.0	760.19± 6.58	1.032	736.34± 6.37	26.90± 0.23	704.79± 6.10
800.0	856.66± 7.32	1.013	845.61± 7.23	30.28± 0.26	807.33± 6.90
794.0	890.86± 7.43	1.009	883.09± 7.37	31.25± 0.26	838.38± 7.00
790.0	892.35±17.70	1.015	879.09±17.44	30.86± 0.61	829.16± 16.45
786.0	926.47± 7.84	1.031	898.19± 7.60	31.28± 0.26	842.92± 7.13
785.0	941.34± 9.33	1.032	911.99± 9.04	31.70± 0.31	858.12± 8.51
784.0	989.76±20.12	1.025	966.05±19.64	33.51± 0.68	915.22± 18.61
783.0	1060.12±11.38	1.010	1050.08±11.27	36.35± 0.39	1005.99± 10.80
782.0	1123.55±26.83	0.989	1136.34±27.14	39.26± 0.94	1102.62± 26.33
781.0	1158.03±10.80	0.971	1192.83±11.12	41.13± 0.38	1169.48± 10.90
780.0	1211.67± 9.98	0.957	1266.56±10.43	43.59± 0.36	1252.62± 10.32
778.0	1273.38± 9.47	0.944	1349.27±10.03	46.25± 0.34	1343.80± 9.99
774.0	1282.06± 9.49	0.938	1366.85±10.12	46.48± 0.34	1361.99± 10.08
770.0	1249.25± 9.26	0.935	1336.51± 9.91	45.08± 0.33	1330.42± 9.86
764.0	1247.24± 9.35	0.932	1338.62±10.04	44.61± 0.33	1331.35± 9.99
760.0	1244.74± 9.58	0.927	1342.60±10.33	44.39± 0.34	1335.30± 10.27
750.0	1219.07±21.50	0.920	1325.56±23.38	42.95± 0.76	1321.82± 23.31
720.0	989.95± 6.62	0.910	1087.59± 7.27	33.15± 0.22	1091.88± 7.30

lower energies, and it was therefore calculated iteratively. The iteration stops then its value changes by not more than 0.1 % in consecutive iterations. The form factor values

$$|F_\pi(s)|^2 = \frac{3s}{\pi\alpha^2\beta^3}\sigma_{\pi\pi}(s), \quad \beta = \sqrt{1 - \frac{4m_\pi^2}{s}}$$

are also listed in Table 1. To evaluate the value of

$$R(s) = \frac{\sigma(e^+e^- \rightarrow \text{hadrons})}{\sigma(e^+e^- \rightarrow \mu^+\mu^-)},$$

which is used in calculating dispersion integrals, the bare cross section $e^+e^- \rightarrow \pi^+\pi^-$ is used (the cross section without vacuum polarization contribution but with the final state radiation taken into account),

$$\sigma_{\pi\pi}^{pol}(s) = \sigma_0(s)|1 - \Pi(s)|^2 \left(1 + \frac{\alpha}{\pi}a(s)\right), \quad (18)$$

where $\Pi(s)$ is the polarization operator calculated according to the Ref. [27] from the known $e^+e^- \rightarrow \text{hadrons}$ cross section [34]. The last factor

Table 1. (Continued)

\sqrt{s} , MeV	$\sigma_{\pi\pi}$, nb	δ_{rad}	σ_0 , nb	$ F_\pi ^2$	$\sigma_{\pi\pi}^{pol}$, nb
690.0	717.99± 7.78	0.915	784.79± 8.50	22.50± 0.24	789.95± 8.56
660.0	515.95± 5.87	0.923	558.83± 6.36	15.07± 0.17	561.19± 6.39
630.0	382.69± 8.35	0.933	410.32± 8.95	10.41± 0.23	411.22± 8.97
600.0	287.18±10.56	0.940	305.50±11.23	7.30± 0.27	305.61± 11.23
580.0	255.24±14.39	0.945	270.24±15.24	6.22± 0.35	269.85± 15.22
560.0	226.60±12.41	0.948	239.01±13.09	5.30± 0.29	238.63± 13.07
550.0	217.52±17.51	0.950	228.99±18.43	4.99± 0.40	228.29± 18.37
540.0	212.67±13.55	0.952	223.47±14.24	4.78± 0.30	222.82± 14.20
530.0	200.04±22.75	0.953	210.00±23.88	4.42± 0.50	209.43± 23.82
520.0	178.13±10.25	0.954	186.73±10.75	3.87± 0.22	186.26± 10.72
510.0	174.28±16.65	0.954	182.60±17.45	3.73± 0.36	181.82± 17.38
500.0	175.22±10.78	0.955	183.52±11.29	3.70± 0.23	182.77± 11.24
480.0	165.18± 9.58	0.955	172.90±10.03	3.41± 0.20	172.29± 9.99
470.0	143.94±13.21	0.955	150.71±13.83	2.94± 0.27	150.22± 13.78
450.0	141.32±14.21	0.954	148.10±14.89	2.86± 0.29	147.42± 14.82
440.0	116.15±15.58	0.953	121.86±16.35	2.35± 0.32	121.34± 16.28
430.0	111.27±12.60	0.952	116.86±13.23	2.26± 0.26	116.41± 13.18
410.0	127.38±19.11	0.949	134.23±20.14	2.64± 0.40	133.84± 20.08
390.0	121.81±22.48	0.944	128.98±23.80	2.65± 0.49	128.76± 23.76

takes the final state radiation into account, and $a(s)$ has the form [35]

$$\begin{aligned}
a(s) = & \frac{1+\beta^2}{\beta} \left[4\text{Li}_2\left(\frac{1-\beta}{1+\beta}\right) + 2\text{Li}_2\left(-\frac{1-\beta}{1+\beta}\right) - \right. \\
& - 3 \ln \frac{2}{1+\beta} \ln \frac{1+\beta}{1-\beta} - 2 \ln \beta \ln \frac{1+\beta}{1-\beta} \left. \right] - \\
& - 3 \ln \frac{4}{1-\beta^2} - 4 \ln \beta + \frac{1}{\beta^3} \left[\frac{5}{4}(1+\beta^2)^2 - 2 \right] \times \\
& \times \ln \frac{1+\beta}{1-\beta} + \frac{3}{2} \frac{1+\beta^2}{\beta^2}.
\end{aligned}$$

Here,

$$\text{Li}_2(x) = - \int_0^x dt \ln(1-t)/t.$$

The values of $\sigma_{\pi\pi}^{pol}(s)$ are listed in Table 1.

The total systematic error of the cross section determination is

$$\sigma_{sys} = \sigma_{eff} \oplus \sigma_{sep} \oplus \sigma_{IL} \oplus \sigma_{rad}.$$

Here, σ_{eff} is the systematic error of the detection efficiency determination, σ_{sep} is the systematic error associated with the $e-\pi$ separation, σ_{IL} is the systematic

error of the integrated luminosity determination, and σ_{rad} is the uncertainty of the radiative correction calculation. The magnitudes of various contributions to the total systematic error are shown in Table 2. The total systematic error of the cross section determinations is $\sigma_{sys} = 1.3\%$ at $\sqrt{s} \geq 420$ MeV and $\sigma_{sys} = 3.2\%$ at $\sqrt{s} < 420$ MeV.

4. THE $e^+e^- \rightarrow \pi^+\pi^-$ CROSS SECTION ANALYSIS

4.1. Theoretical framework

In the framework of the vector meson dominance model, the cross section of the $e^+e^- \rightarrow \pi^+\pi^-$ process is

$$\sigma_{\pi\pi}(s) = \frac{4\pi\alpha^2}{s^{3/2}} P_{\pi\pi}(s) |A_{\pi\pi}(s)|^2. \quad (19)$$

Here, $P_{\pi\pi}(s)$ is the phase space factor:

$$P_{\pi\pi}(s) = q_\pi^3(s), \quad q_\pi(s) = \frac{1}{2} \sqrt{s - 4m_\pi^2}.$$

Table 2. Various contributions to the systematic error of the $e^+e^- \rightarrow \pi^+\pi^-$ cross section determination. σ_{sys} is the total systematic error and $\sigma_{eff} = \sigma_{E>50} \oplus \sigma_{nucl} \oplus \sigma_{\theta}$ is the systematic inaccuracy of the detection efficiency determination

Error	Contribution at $\sqrt{s} \geq 420$ MeV	Contribution at $\sqrt{s} < 420$ MeV
$\sigma_{E>50}$	0.6 %	3.0 %
σ_{nucl}	0.2 %	0.2 %
σ_{θ}	0.8 %	0.8 %
σ_{eff}	1.0 %	3.1 %
σ_{sep}	0.5 %	0.5 %
σ_{IL}	0.5 %	0.5 %
σ_{rad}	0.2 %	0.2 %
σ_{sys}	1.3 %	3.2 %

The amplitudes of the $\gamma^* \rightarrow \pi^+\pi^-$ transition are given by

$$|A_{\pi\pi}(s)|^2 = \left| \sqrt{\frac{3}{2}} \frac{1}{\alpha} \times \sum_{V=\rho,\omega,\rho',\rho''} \frac{\Gamma_V m_V^3 \sqrt{m_V} \sigma(V \rightarrow \pi^+\pi^-)}{D_V(s)} \times \frac{e^{i\phi_{\rho V}}}{\sqrt{q_\pi^3(m_V)}} \right|^2, \quad (20)$$

where

$$D_V(s) = m_V^2 - s - i\sqrt{s}\Gamma_V(s),$$

$$\Gamma_V(s) = \sum_f \Gamma(V \rightarrow f, s).$$

Here, f denotes the final state of the V vector meson decay, m_V is the vector meson mass, and $\Gamma_V = \Gamma_V(m_V)$. The following forms of the energy dependence of the vector meson total widths were used:

$$\Gamma_\omega(s) = \frac{m_\omega^2}{s} \frac{q_\pi^3(s)}{q_\pi^3(m_\omega)} \Gamma_\omega B(\omega \rightarrow \pi^+\pi^-) + \frac{q_\pi^3(s)}{q_\pi^3(m_\omega)} \Gamma_\omega B(\omega \rightarrow \pi^0\gamma) + \frac{W_{\rho\pi}(s)}{W_{\rho\pi}(m_\omega)} \Gamma_\omega B(\omega \rightarrow 3\pi),$$

$$\Gamma_V(s) = \frac{m_V^2}{s} \frac{q_\pi^3(s)}{q_\pi^3(m_V)} \Gamma_V, \quad V = \rho, \rho', \rho''.$$

Here,

$$q_{\pi\gamma} = \frac{s - m_\pi^2}{2\sqrt{s}},$$

$W_{\rho\pi}(s)$ is the phase-space factor for the $\rho\pi \rightarrow \pi^+\pi^-\pi^0$ final state [30–32]. In the energy dependence of the ρ, ρ', ρ'' mesons widths, only the $V \rightarrow \pi^+\pi^-$ decays were taken into account. This approach is justified in the energy region $\sqrt{s} < 1000$ MeV. Nowadays, the ρ', ρ'' decays are rather poorly known, and therefore the same approximation was also used for fitting the data above 1000 MeV. The ω -meson mass and width were taken from the SND measurements: $m_\omega = 782.79$ MeV and $\Gamma_\omega = 8.68$ MeV [31].

The relative decay probabilities were calculated as

$$B(V \rightarrow X) = \frac{\sigma(V \rightarrow X)}{\sigma(V)}, \quad \sigma(V) = \sum_X \sigma(V \rightarrow X),$$

$$\sigma(V \rightarrow X) = \frac{12\pi B(V \rightarrow e^+e^-) B(V \rightarrow X)}{m_V^2}.$$

In the analysis presented here, we have used $\sigma(\omega \rightarrow \pi^0\gamma) = 155.8$ nb and $\sigma(\omega \rightarrow 3\pi) = 1615$ nb obtained in the SND experiments [31, 36].

The parameter $\phi_{\rho V}$ is the relative interference phase between the vector mesons V and ρ , and hence $\phi_{\rho\rho} = 0$. The phases $\phi_{\rho V}$ can deviate from 180° or 0° , and their values can be energy-dependent due to mixing between vector mesons. The phases $\phi_{\rho\rho'}$ and $\phi_{\rho\rho''}$ were fixed at 180° and 0° , because these values are consistent with the existing experimental data for the $e^+e^- \rightarrow \pi^+\pi^-$ reaction.

Taking the $\rho - \omega$ mixing into account, the $\omega \rightarrow \pi^+\pi^-$ and $\rho \rightarrow \pi^+\pi^-$ transition amplitudes can be written as [37, 38]

$$A_{\omega \rightarrow \pi^+\pi^-} + A_{\rho \rightarrow \pi^+\pi^-} = \frac{g_{\gamma\rho}^{(0)} g_{\rho\pi\pi}^{(0)}}{D_\rho(s)} \left[1 - \frac{g_{\gamma\omega}^{(0)}}{g_{\gamma\rho}^{(0)}} \varepsilon(s) \right] + \frac{g_{\gamma\omega}^{(0)} g_{\rho\pi\pi}^{(0)}}{D_\omega(s)} \left[\varepsilon(s) + \frac{g_{\omega\pi\pi}^{(0)}}{g_{\rho\pi\pi}^{(0)}} \right], \quad (21)$$

where

$$\varepsilon(s) = \frac{-\Pi_{\rho\omega}}{D_\omega(s) - D_\rho(s)},$$

$$|g_{V\gamma}| = \left[\frac{3m_V^3 \Gamma_V B(V \rightarrow e^+e^-)}{4\pi\alpha} \right]^{1/2},$$

$$|g_{V\pi\pi}| = \left[\frac{6\pi m_V^2 \Gamma_V B(V \rightarrow \pi^+\pi^-)}{q_\pi^3(m_V)} \right]^{1/2}.$$

The superscript (0) denotes the coupling constants of the bare, unmixed state. $\Pi_{\rho\omega}$ is the polarization operator of the $\rho - \omega$ mixing:

$$\Pi_{\rho\omega}(s) = \text{Re}(\Pi_{\rho\omega}(s)) + i \text{Im}(\Pi_{\rho\omega}(s)), \quad (22)$$

and $\text{Im}(\Pi_{\rho\omega}(s))$ can be written as

$$\text{Im}(\Pi_{\rho\omega}(s)) = \sqrt{s} \left\{ \frac{g_{\rho\pi\pi}^{(0)} g_{\omega\pi\pi}^{(0)} q_{\pi}^3(s)}{6\pi s} + \frac{g_{\rho\pi\gamma}^{(0)} g_{\omega\pi\gamma}^{(0)} q_{\pi\gamma}^3(s) + g_{\rho\eta\gamma}^{(0)} g_{\omega\eta\gamma}^{(0)} q_{\eta\gamma}^3(s)}{3} \right\}, \quad (23)$$

where

$$g_{VP\gamma} = \left[\frac{3\Gamma_V B(V \rightarrow P\gamma)}{q_{P\gamma}^3(m_V)} \right]^{1/2}.$$

We neglected the contributions to $\text{Im}(\Pi_{\rho\omega}(s))$ due to the VP intermediate state ($V = \omega, \rho, P = \pi, \eta$). The real part $\text{Re}(\Pi_{\rho\omega}(s))$ can be represented as

$$\text{Re}(\Pi_{\rho\omega}(s)) = \text{Re}(\Pi_{\rho\omega}^\gamma(s)) + \text{Re}(\Pi_{\rho\omega}'(s)), \quad (24)$$

where

$$\text{Re}(\Pi_{\rho\omega}^\gamma(s)) = \frac{-4\pi g_{\rho\gamma}^{(0)} g_{\omega\gamma}^{(0)}}{s} \quad (25)$$

is the one-photon contribution to $\text{Re}(\Pi_{\rho\omega}(s))$. We assume that the energy dependence of $\text{Re}(\Pi_{\rho\omega}'(s))$ is negligible, and can then be expressed by using the measured branching ratio

$$B(\omega \rightarrow \pi^+\pi^-) = \frac{\Gamma_\rho(m_\omega)}{\Gamma_\omega} \left| \varepsilon(m_\omega) + \frac{g_{\omega\pi\pi}^{(0)}}{g_{\rho\pi\pi}^{(0)}} \right|^2 \quad (26)$$

as

$$\begin{aligned} \text{Re}(\Pi_{\rho\omega}') &= \frac{4\pi g_{\rho\gamma}^{(0)} g_{\omega\gamma}^{(0)}}{m_\omega^2} + \frac{g_{\omega\pi\pi}^{(0)}}{g_{\rho\pi\pi}^{(0)}} (m_\omega^2 - m_\rho^2) + \\ &+ \left\{ \frac{\Gamma_\omega B(\omega \rightarrow \pi^+\pi^-)}{\Gamma_\rho(m_\omega)} \left| D_\omega(m_\omega) - D_\rho(m_\omega) \right|^2 - \right. \\ &- \left[\frac{g_{\rho\pi\gamma}^{(0)} g_{\omega\pi\gamma}^{(0)} q_{\pi\gamma}^3(m_\omega) + g_{\rho\eta\gamma}^{(0)} g_{\omega\eta\gamma}^{(0)} q_{\eta\gamma}^3(m_\omega)}{3} + \right. \\ &\left. \left. + \frac{g_{\omega\pi\pi}^{(0)}}{g_{\rho\pi\pi}^{(0)}} m_\omega \Gamma_\omega \right]^2 \right\}^{1/2}. \quad (27) \end{aligned}$$

Equation (21) can be rewritten as

$$\begin{aligned} A_{\omega \rightarrow \pi^+\pi^-} + A_{\rho \rightarrow \pi^+\pi^-} &= \sqrt{\frac{3}{2}} \frac{1}{\alpha} \times \\ &\times \sum_{V=\omega,\rho} \frac{\Gamma_V m_V^3}{D_V(s)} \frac{\sqrt{m_V \sigma(V \rightarrow \pi^+\pi^-)}}{D_V(s)} \times \\ &\times \frac{f_{V\pi\pi}(s)}{\sqrt{q_\pi(m_V)}}, \quad (28) \end{aligned}$$

where

$$f_{V\pi\pi}(s) = \frac{r_{V\pi\pi}(s)}{r_{V\pi\pi}(m_V)},$$

and

$$r_{\rho\pi\pi}(s) = 1 - \frac{g_{\gamma\omega}^{(0)}}{g_{\gamma\rho}^{(0)}} \varepsilon(s), \quad r_{\omega\pi\pi}(s) = \varepsilon(s) + \frac{g_{\omega\pi\pi}^{(0)}}{g_{\rho\pi\pi}^{(0)}}.$$

The theoretical value of the phase $\phi_{\rho\omega}$ can be calculated from the above expressions:

$$\phi_{\rho\omega} = \arg(f_{\omega\pi\pi}(m_\omega)) - \arg(f_{\rho\pi\pi}(m_\rho)) \approx 101^\circ.$$

The phase $\phi_{\rho\omega}$ is almost independent of energy. In this calculation, we assumed that the $\omega \rightarrow \pi^+\pi^-$ transition proceeds only via the $\rho - \omega$ mixing, that is, $g_{\omega\pi\pi}^{(0)} = 0$. To determine the $g_{\rho\pi\pi}^{(0)}$, $g_{\gamma V}^{(0)}$, and $g_{VP\gamma}^{(0)}$ coupling constants, the corresponding measured decay widths were used.

4.2. Fit to the experimental data

The ρ' and ρ'' parameters were determined from the fit to the $e^+e^- \rightarrow \pi^+\pi^-$ cross section measured in the energy region $\sqrt{s} < 2400$ MeV by OLYA and DM2 detectors [17, 39], together with the isovector part of the $e^+e^- \rightarrow \pi^+\pi^-$ cross section calculated by assuming the CVC hypothesis from the spectral function of the $\tau^- \rightarrow \pi^- \pi^0 \nu_\tau$ decay measured by CLEO II [5],

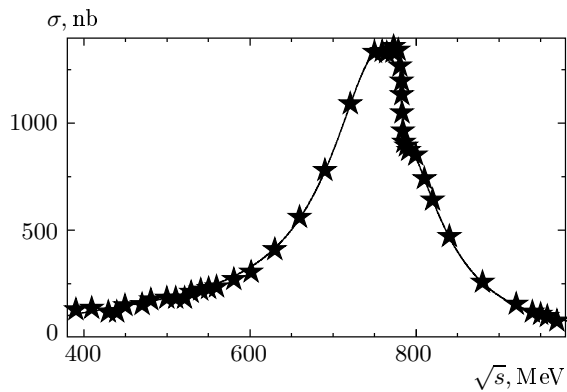
$$\begin{aligned} \sigma_{\pi\pi}(m_i) &= \frac{4(\pi\alpha)^2}{m_i} \frac{B(\tau \rightarrow \pi\pi^0\nu_\tau)}{B(\tau \rightarrow e\bar{\nu}_e\nu_\tau)} \frac{m_\tau^8}{12\pi|V_{ud}|^2} \frac{1}{S_{EW}} \times \\ &\times \frac{1}{m_i(m_\tau^2 - m_i^2)^2(m_\tau^2 + 2m_i^2)} \frac{1}{N} \frac{N_i}{\Delta m_i}, \quad (29) \end{aligned}$$

where m_i is the central value of the $\pi^-\pi^0$ pair invariant mass for the i th bin, Δm_i is the bin width, N_i is the number of entries in the i th bin, N is the total number of entries, $|V_{ud}|$ is the CKM matrix element, and $S_{EW} = 1.0194$ is the radiative correction [3, 5, 40].

The obtained ρ' and ρ'' parameters were used in the fitting to the SND data (Table 3, Fig. 21). The free parameters of the fit were m_ρ , Γ_ρ , $\sigma(\rho \rightarrow \pi^+\pi^-)$, $\sigma(\omega \rightarrow \pi^+\pi^-)$, $\phi_{\rho\omega}$ and $\sigma(\rho' \rightarrow \pi^+\pi^-)$. The first fit was performed with $\sigma(\rho'' \rightarrow \pi^+\pi^-)$, ρ' and ρ'' masses, and widths fixed at the values obtained from the fit to the CLEO II and DM2 data. The second and third fits were done without the ρ'' meson. The ρ' mass and width were fixed by using the results of the fit to the CLEO II and DM2 data (the second variant in the Table 3) and to the OLYA data (the third variant in Table 3). The values of the ρ and ω parameters exhibit a rather weak model dependence.

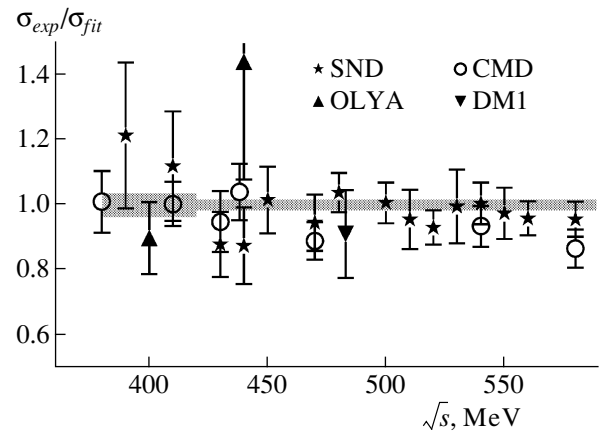
Table 3. Fit results. The column number N corresponds to the different choices of the ρ' and ρ'' parameters

N	1	2	3
m_ρ , MeV	774.9 ± 0.4	774.9 ± 0.4	774.9 ± 0.4
Γ_ρ , MeV	146.2 ± 0.8	146.4 ± 0.8	146.3 ± 0.8
$\sigma(\rho \rightarrow \pi^+ \pi^-)$, nb	1222 ± 7	1218 ± 7	1219 ± 7
$\sigma(\omega \rightarrow \pi^+ \pi^-)$, nb	30.2 ± 1.4	30.3 ± 1.4	30.3 ± 1.4
$\phi_{\rho\omega}$, degree	113.6 ± 1.3	113.4 ± 1.3	113.5 ± 1.3
$m_{\rho'}$, MeV	1403	1403	1360
$\Gamma_{\rho'}$, MeV	455	455	430
$\sigma(\rho' \rightarrow \pi^+ \pi^-)$, nb	3.8 ± 0.3	1.8 ± 0.2	1.9 ± 0.2
$m_{\rho''}$, MeV	1756		
$\Gamma_{\rho''}$, MeV	245		
$\sigma(\rho'' \rightarrow \pi^+ \pi^-)$, nb	1.7		
χ^2/N_{df}	50.2/39	48.8/39	49.4/39

**Fig. 21.** The $e^+e^- \rightarrow \pi^+\pi^-$ cross section. Stars are the SND data obtained in this work, the curve is the fit result

5. DISCUSSION

The comparison of the $e^+e^- \rightarrow \pi^+\pi^-$ cross section obtained in the SND experiment with other results [8, 9, 17–19] is shown in Figs. 22, 23, 24, and 25. In the energy region $\sqrt{s} < 600$ MeV, all experimental data are in agreement (Fig. 22). Above 600 MeV, the OSPK(ORSAY-ACO)[8] and DM1 [9] points lie about 10 % lower than the SND ones (Fig. 23). The SND cross section exceeds the OLYA and CMD measurements [17] by 6 ± 1 % in this energy region (Fig. 24). The systematic error of OLYA measurement is 4 % and the OLYA data agree with the SND result. The systematic uncertainty of the CMD result is 2 %, and hence the differ-

**Fig. 22.** The ratio of the $e^+e^- \rightarrow \pi^+\pi^-$ cross section obtained in different experiments to the fit curve (Fig. 21). The shaded area shows the systematic error of the SND measurements. The SND (\star , this work), CMD (\circ), OLYA (\blacktriangle) and DM1 (\blacktriangledown) [9, 17] results are presented

ence between the SND and CMD results is about 2.5 of the joint systematic error. At the same time, the SND and CMD data below 600 MeV agree well (Fig. 22). The average deviation between CMD2 [18] and SND data is 1.4 ± 0.5 %, the systematic inaccuracies of these measurements are 0.6 % and 1.3 % respectively. In the KLOE experiment at the ϕ -factory DAFΦNE, the form factor $|F_\pi(s)|^2$ was measured by using the «radiative return» method with the systematic error 0.9 % [19]. In Ref. [19], the bare form factor is listed. In order to

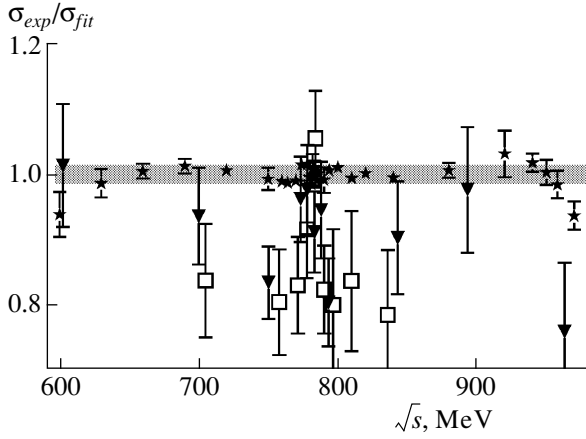


Fig. 23. The ratio of the $e^+e^- \rightarrow \pi^+\pi^-$ cross section obtained in different experiments to the fit curve (Fig. 21). The shaded area shows the systematic error of the SND measurements. The SND (*, this work), DM1 (\blacktriangledown), and OSPK (\square) [8, 9] results are presented

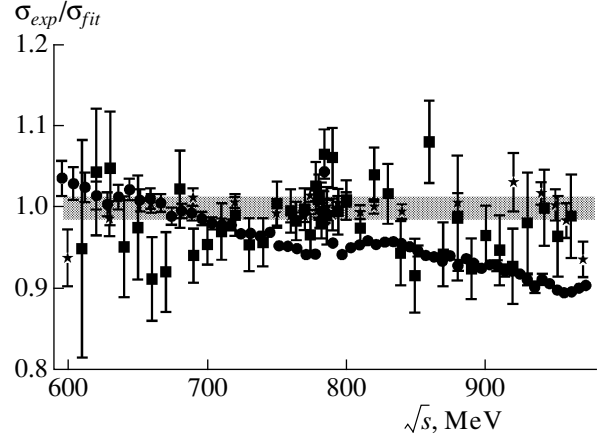


Fig. 25. The ratio of the $e^+e^- \rightarrow \pi^+\pi^-$ cross section obtained in different experiments to the fit curve (Fig. 21). The shaded area shows the systematic error of the SND measurements. The SND (*, this work), CMD2 (\blacksquare) and KLOE (\bullet) [18, 19] results are presented

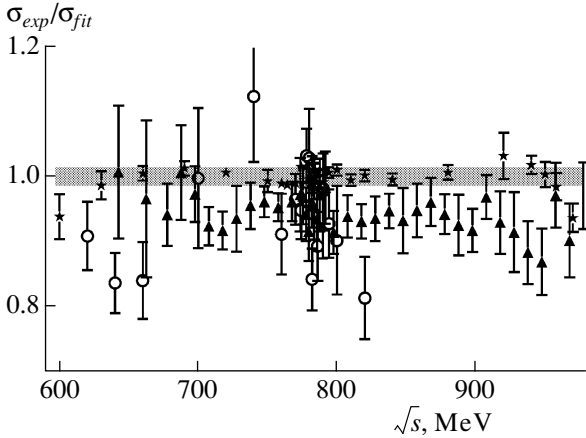


Fig. 24. The ratio of the $e^+e^- \rightarrow \pi^+\pi^-$ cross section obtained in different experiments to the fit curve (Fig. 21). The shaded area shows the systematic error of the SND measurements. The SND (*, this work), OLYA (\blacktriangle), and CMD (\circ) [17] results are presented

compare the KLOE result with the SND one, we therefore appropriately dressed the form factor. The results of this comparison are shown in Fig. 25. The KLOE measurement is in conflict with the SND result as well as with the CMD2 one.

The ρ -meson parameters m_ρ , Γ_ρ , $\sigma(\rho \rightarrow \pi^+\pi^-)$ were determined from the study of the $e^+e^- \rightarrow \pi^+\pi^-$ cross section. The ρ meson mass and width were found to be

$$m_\rho = 774.9 \pm 0.4 \pm 0.5 \text{ MeV},$$

$$\Gamma_\rho = 146.5 \pm 0.8 \pm 1.5 \text{ MeV}.$$

The systematic error is related to the accuracy of the collider energy determination, to the model uncertainty and to the error of the cross section determination. The ρ -meson parameters were studied in other e^+e^- experiments by using the processes $e^+e^- \rightarrow \pi^+\pi^-$ [17, 18], $e^+e^- \rightarrow \rho\pi \rightarrow \pi^+\pi^-\pi^0$ [32, 41] and the $\tau^- \rightarrow \pi^-\pi^0\nu_\tau$ decay [3, 5]. The SND results are in agreement with these measurements, as is shown in Figs. 26 and 27.

The parameter $\sigma(\rho \rightarrow \pi^+\pi^-)$ was found to be

$$\sigma(\rho \rightarrow \pi^+\pi^-) = 1220 \pm 7 \pm 16 \text{ nb},$$

which corresponds to

$$\begin{aligned} B(\rho \rightarrow e^+e^-)B(\rho \rightarrow \pi^+\pi^-) &= \\ &= (4.991 \pm 0.028 \pm 0.066) \cdot 10^{-5}, \end{aligned}$$

$$\Gamma(\rho \rightarrow e^+e^-) = 7.31 \pm 0.021 \pm 0.11 \text{ keV}.$$

The systematic error includes systematic uncertainties in the cross section measurement and the model dependence. A comparison of the $\Gamma(\rho \rightarrow e^+e^-)$ obtained in this work with other experimental results [8, 17, 18] and with the PDG world average [42] is shown in Fig. 28. The SND result exceeds all previous measurements. It differs by about 1.5 standard deviations from the CMD2 measurement [18] and by 2 standard deviations from the PDG world average [42]. The difference of the ρ -meson leptonic widths obtained by SND

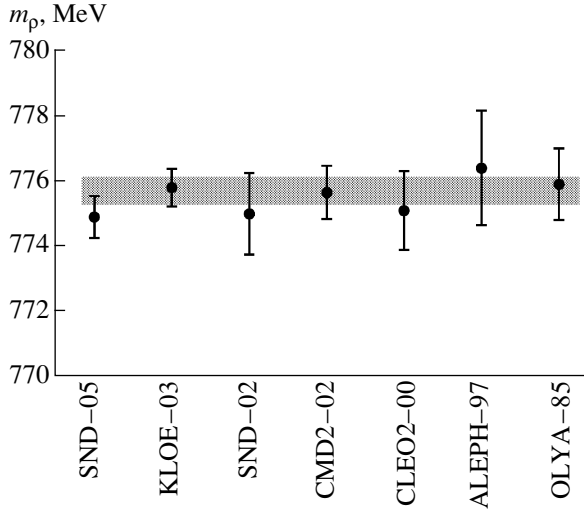


Fig. 26. The ρ -meson mass m_ρ measured in this work (SND-05) and in Refs. [3, 5, 17, 18, 32, 41]. The shaded area shows the average of the previous results

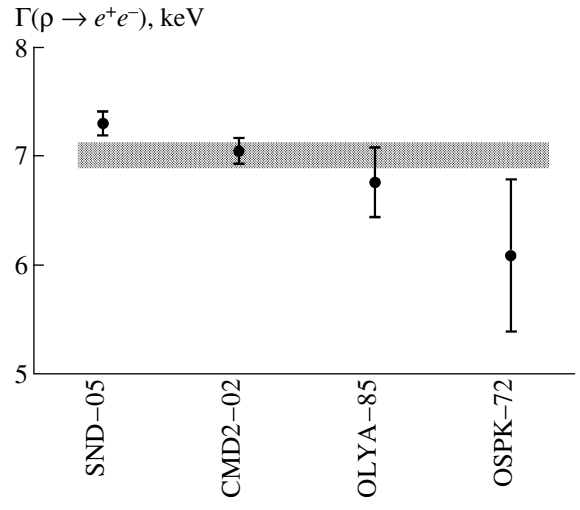


Fig. 28. The value of $\Gamma(\rho \rightarrow e^+e^-)$ obtained in this work (SND-05) and in Refs. [8, 17, 18]. The shaded area shows the world average value [42]

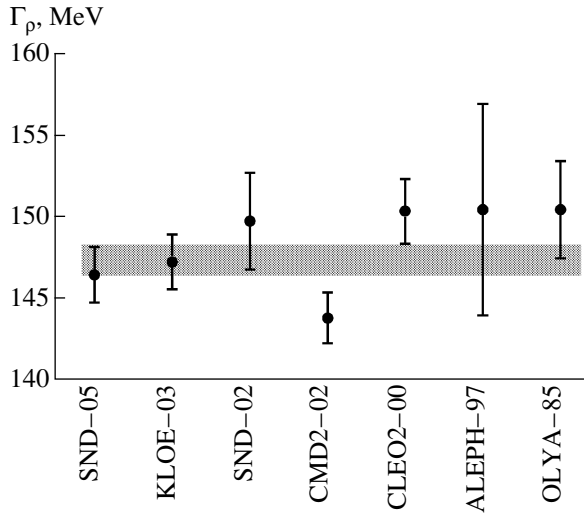


Fig. 27. The ρ meson width Γ_ρ measured in this work (SND-05) and in Refs. [3, 5, 17, 18, 32, 41]. The shaded area shows the average of the previous results

and CMD2 should be attributed mainly to the difference in the total widths of the ρ -meson rather than to the difference in the cross section values. The value $\sigma(\rho \rightarrow \pi^+\pi^-) = 1198 \text{ nb}$, which can be obtained by using the CMD2 cross section data reported in Ref. [18], agrees with the SND result within the measurements errors.

The parameter $\sigma(\omega \rightarrow \pi^+\pi^-)$ was found to be

$$\sigma(\omega \rightarrow \pi^+\pi^-) = 29.9 \pm 1.2 \pm 1.0 \text{ nb},$$

which corresponds to

$$\begin{aligned} B(\omega \rightarrow e^+e^-)B(\omega \rightarrow \pi^+\pi^-) &= \\ &= (1.247 \pm 0.062 \pm 0.042) \cdot 10^{-6}. \end{aligned}$$

The systematic error is related to the model dependence, to the error of the cross section determination, and to the accuracy of the collider energy determination. In the previous studies of the $e^+e^- \rightarrow \pi^+\pi^-$ reaction, the relative probability of the $\omega \rightarrow \pi^+\pi^-$ decay was also reported. The comparison of $B(\omega \rightarrow \pi^+\pi^-) = 0.0175 \pm 0.0011$ obtained by using the SND data and the PDG value of the $\omega \rightarrow e^+e^-$ decay width [42] with the results of other experiments is shown in Fig. 29. The SND result is most precise.

The phase $\phi_{\rho\omega}$ was found to be

$$\phi_{\rho\omega} = 113.5^\circ \pm 1.3^\circ \pm 1.7^\circ.$$

This value differs by six standard deviations from 101° expected under the assumption that the $\omega \rightarrow \pi^+\pi^-$ transition proceeds through the $\rho - \omega$ mixing mechanism. If the ratio $g_{\omega\pi\pi}^{(0)}/g_{\rho\pi\pi}^{(0)}$ is the free parameter of the fit instead of the phase $\phi_{\rho\omega}$, it follows that

$$\frac{g_{\omega\pi\pi}^{(0)}}{g_{\rho\pi\pi}^{(0)}} = 0.11 \pm 0.01.$$

This ratio corresponds to the too large direct transition width

$$\Gamma^{(0)}(\omega \rightarrow \pi^+\pi^-) = 1.82 \pm 0.33 \text{ MeV},$$

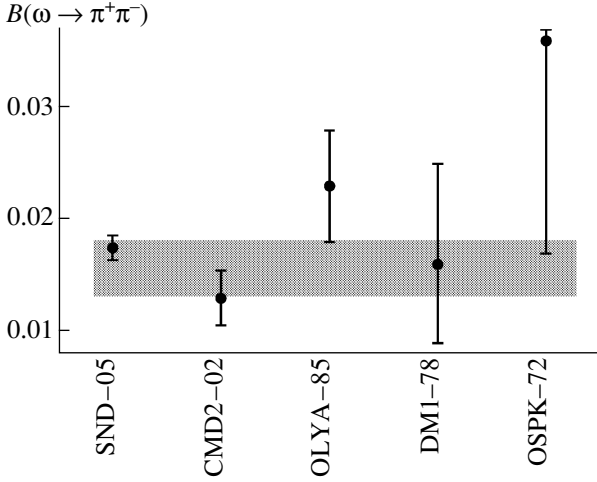


Fig. 29. The value of $B(\omega \rightarrow \pi^+\pi^-)$ obtained in this work (SND-05) and in Refs. [8, 9, 17, 18]. The shaded area shows the world average value [42]

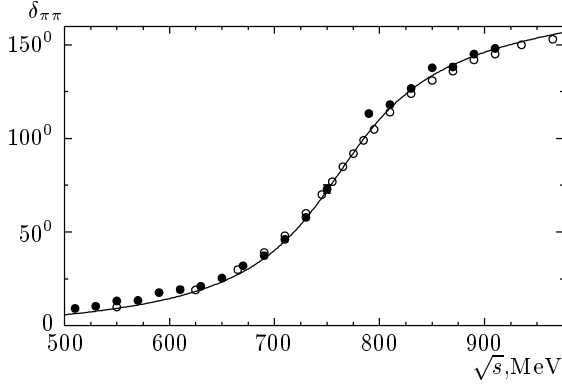


Fig. 30. The $\pi\pi$ scattering phase in the P -wave. Dots and circles are the results of the phase measurements in Refs. [43, 44] by using the reaction $\pi N \rightarrow \pi\pi N$. The curve is the phase of the amplitude $A_{\rho \rightarrow \pi\pi} + A_{\rho' \rightarrow \pi^+\pi^-}$ obtained from the fit to the SND data presented in this work

while the natural expectation is

$$\Gamma^{(0)}(\omega \rightarrow \pi^+\pi^-) \approx \alpha^2 \Gamma_\rho \approx 8 \text{ keV.}$$

We note that the analysis of the OLYA and CMD2 data [17, 18] gives similar values of the $\phi_{\rho\omega}$ phase. This result can point out that a considerable direct transition $\omega \rightarrow \pi^+\pi^-$ exists. On the other hand, this discrepancy can also be attributed to inadequacies of the applied theoretical model.

The comparison of the phase $\arg(A_{\rho \rightarrow \pi^+\pi^-} + A_{\rho' \rightarrow \pi^+\pi^-})$ with the $\pi\pi$ scattering phase in the P -wave [43, 44] is shown in Fig. 30. These phases must

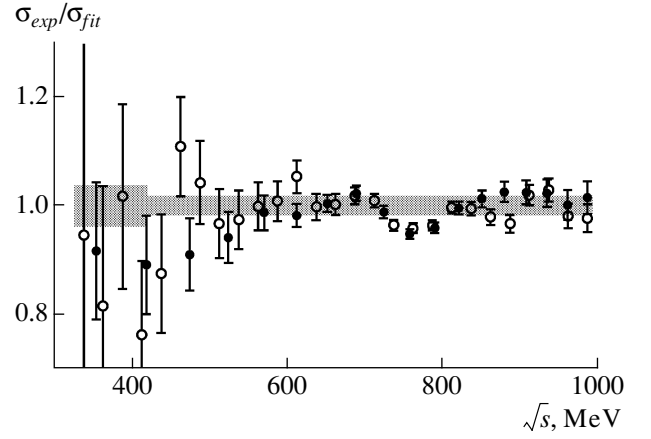


Fig. 31. The ratio of the $e^+e^- \rightarrow \pi^+\pi^-$ cross section calculated from the $\tau^- \rightarrow \pi^-\pi^0\nu_\tau$ decay spectral function measured in Refs. [3, 5] (\circ — CLEOII, \bullet — ALEPH) to the isovector part of the $e^+e^- \rightarrow \pi^+\pi^-$ cross section measured in this work. The shaded area shows the joint systematic error

be equal in the purely elastic scattering region. The agreement is satisfactory, and in any case, no essential difference is observed in the energy region $\sqrt{s} \approx m_\rho$.

The comparison of the $e^+e^- \rightarrow \pi^+\pi^-$ cross section obtained under the CVC hypothesis from the τ spectral function of the $\tau^- \rightarrow \pi^-\pi^0\nu_\tau$ decay [3, 5] with the isovector part of the cross section measured in this work is shown in Fig. 31. The cross section obtained by SND was undressed from the vacuum polarization and the contribution from the $\omega \rightarrow \pi^+\pi^-$ decay was excluded. The cross section calculated from the τ spectral function was multiplied by the coefficient that takes the difference of the π^\pm and π^0 masses into account:

$$\delta = \left(\frac{q_\pi(s)}{q_{\pi^\pm}(s)} \right)^3 \frac{|A_{\pi^+\pi^-}(s)|^2}{|A_{\pi^0\pi^\pm}(s)|^2},$$

$$q_{\pi^\pm}(s) = \frac{1}{2\sqrt{s}} [(s - (m_{\pi^0} + m_{\pi^\pm})^2)(s - (m_{\pi^0} - m_{\pi^\pm})^2)]^{1/2}.$$

The average deviation of the SND and τ data is about 1.5%. For almost all energy points, this deviation is within the joint systematic error (about 1.6%). The 10% difference between the e^+e^- and τ data at $\sqrt{s} > 800$ MeV, which was claimed in Ref. [45], is absent.

Using the $\sigma_{\pi\pi}^{pol}(s)$ cross section (Table 1), the contribution to the anomalous magnetic moment of the muon, due to the $\pi^+\pi^-(\gamma)$ intermediate state in the vacuum polarization, was calculated via the dispersion integral,

$$a_\mu(\pi\pi, 390\text{MeV} \leq \sqrt{s} \leq 970 \text{ MeV}) = \\ = \left(\frac{\alpha m_\mu}{3\pi}\right)^2 \int_{s_{min}}^{s_{max}} \frac{R(s)K(s)}{s^2} ds,$$

where $s_{max} = 970 \text{ MeV}$, $s_{min} = 390 \text{ MeV}$, $K(s)$ is the known kernel, and

$$R(s) = \frac{\sigma_{\pi\pi}^{pol}}{\sigma(e^+e^- \rightarrow \mu^+\mu^-)}, \\ \sigma(e^+e^- \rightarrow \mu^+\mu^-) = \frac{4\pi\alpha^2}{3s}.$$

The integral was evaluated by using the trapezoidal rule. To take the numerical integration errors into account, the correction method suggested in Ref. [46] was applied. As a result, we obtained

$$a_\mu(\pi\pi, 390 \text{ MeV} \leq \sqrt{s} \leq 970 \text{ MeV}) = \\ = (488.7 \pm 2.6 \pm 6.6) \cdot 10^{-10}.$$

This is about 70 % of the total hadronic contribution to the anomalous magnetic moment of the muon $(g-2)/2$.

If the integration is performed for the energy region corresponding to the CMD2 measurements [18], then the result is

$$a_\mu(\pi\pi) = (385.6 \pm 5.2) \cdot 10^{-10},$$

which is 1.8 % (one standard deviation) higher than the CMD2 result:

$$a_\mu(\pi\pi) = (378.6 \pm 3.5) \cdot 10^{-10}.$$

Hence, no considerable difference between the SND and CMD2 results is observed.

6. CONCLUSION

The cross section of the process $e^+e^- \rightarrow \pi^+\pi^-$ was measured in the SND experiment at the VEPP-2M collider in the energy region $390 < \sqrt{s} < 980 \text{ MeV}$ with the accuracy 1.3 % at $\sqrt{s} \geq 420 \text{ MeV}$ and 3.4 % at $\sqrt{s} < 420 \text{ MeV}$. The measured cross section was analyzed in the framework of the generalized vector meson dominance model. The following ρ -meson parameters were obtained:

$$m_\rho = 774.9 \pm 0.4 \pm 0.5 \text{ MeV},$$

$$\Gamma_\rho = 146.5 \pm 0.8 \pm 1.5 \text{ MeV},$$

$$\sigma(\rho \rightarrow \pi^+\pi^-) = 1220 \pm 7 \pm 16 \text{ nb}.$$

The parameters of the G -parity suppressed process $e^+e^- \rightarrow \omega \rightarrow \pi^+\pi^-$ were measured with high precision. The measured value

$$\sigma(\omega \rightarrow \pi^+\pi^-) = 29.9 \pm 1.4 \pm 1.0 \text{ nb}$$

corresponds to the relative probability

$$B(\omega \rightarrow \pi^+\pi^-) = 1.75 \pm 0.11 \text{ \%}.$$

The relative interference phase between the ρ and ω mesons was found to be

$$\phi_{\rho\omega} = 113.5^\circ \pm 1.3^\circ \pm 1.7^\circ.$$

This result is in conflict with the naive expectation $\phi_{\rho\omega} = 101^\circ$ from the $\rho - \omega$ mixing. The SND result agrees with the cross section calculated from the τ spectral function data within the accuracy of the measurements. Using the measured cross section, the contribution to the anomalous magnetic moment of the muon due to the $\pi^+\pi^-(\gamma)$ intermediate state in the vacuum polarization was calculated:

$$a_\mu(\pi\pi, 390 \text{ MeV} \leq \sqrt{s} \leq 970 \text{ MeV}) = \\ = (488.7 \pm 2.6 \pm 6.6) \cdot 10^{-10}.$$

The authors are grateful to N. N. Achasov for useful discussions. The work is supported in part by the RFBR grants №№ 04-02-16181-a, 04-02-16184-a, 05-02-16250-a, and LSS-1335.2003.2.

REFERENCES

1. H. N. Brown et al., Phys. Rev. Lett. **86**, 2227 (2001).
2. G. W. Bennet et al., Phys. Rev. Lett. **92**, 161802 (2004).
3. R. Barate et al., Z. Phys. C **76**, 15 (1997).
4. K. Ackerstaff et al., Eur. Phys. J. C **7**, 571 (1999).
5. S. Anderson et al., Phys. Rev. D **61**, 112002 (2000).
6. J. E. Augustin et al., Phys. Rev. Lett. **20**, 126 (1968); J. E. Augustin et al., Nuovo Cim. Lett. **2**, 214 (1969); J. E. Augustin et al., Phys. Lett. B **28**, 508 (1969).
7. V. L. Auslender et al., Phys. Lett. B **25**, 433 (1967); V. L. Auslender et al., Yad. Fiz. **9**, 114 (1969).
8. D. Benaksas et al., Phys. Lett. B **39**, 289 (1972).
9. A. Quenzer et al., Phys. Lett. B **76**, 512 (1978).
10. I. B. Vasserman et al., Yad. Fiz. **28**, 968 (1978).

11. A. D. Bukin et al., Phys. Lett. B **73**, 226 (1978).
12. I. B. Vasserman et al., Yad. Fiz. **30**, 999 (1979).
13. I. B. Vasserman et al., Yad. Fiz. **33**, 709 (1981).
14. L. M. Kurdadze et al., Pisma Zh. Eksp. Teor. Fiz. **37**, 613 (1983).
15. L. M. Kurdadze et al., Yad. Fiz. **40**, 451 (1984).
16. S. R. Amendolia et al., Phys. Lett. B **138**, 454 (1984).
17. L. M. Barkov et al., Nucl. Phys. B **256**, 365 (1985).
18. R. R. Akhmetshin et al., Phys. Lett. B **527**, 161 (2002); R. R. Akhmetshin et al., Phys. Lett. B **578**, 285 (2004).
19. A. Aloisio et al., Phys. Lett. B **606**, 12 (2005).
20. M. N. Achasov et al., Nucl. Instr. and Meth. A **449**, 125 (2000).
21. A. N. Skrinsky, in *Proc. of Workshop on Physics and Detectors for DAΦNE*, Frascati, Italy (1995), p. 3.
22. A. D. Bukin et al., in *Proc. of Workshop on Detector and Event Simulation in High Energy Physics*, Amsterdam, Netherlands (1991), p. 79.
23. A. D. Bukin and N. A. Grozina, Comp. Phys. Comm. **78**, 287 (1994).
24. K. Hänssgen and S. Ritter, Comp. Phys. Comm. **31**, 411 (1984); K. Hänssgen and J. Raunft, Comp. Phys. Comm. **39**, 37 (1986); K. Hänssgen and J. Raunft, Comp. Phys. Comm. **39**, 53 (1986); K. Hänssgen, Nucl. Sc. and Eng. **95**, 137 (1987).
25. A. D. Bukin et al., Report of Budker INP №92–93, Novosibirsk (1992).
26. F. A. Berends and R. Kleiss, Nucl. Phys. B **228**, 537 (1983).
27. A. B. Arbuzov et al., JHEP **10**, 001 (1997).
28. A. B. Arbuzov et al., JHEP **10**, 006 (1997).
29. B. H. Denby, Comput. Phys. Commun. **49**, 429 (1988).
30. M. N. Achasov et al., Phys. Rev. D **63**, 072002 (2001).
31. M. N. Achasov et al., Phys. Rev. D **68**, 052006 (2003).
32. M. N. Achasov et al., Phys. Rev. D **65**, 032002 (2002).
33. S. Jadach, W. Placzek, and B. F. L. Ward, Phys. Lett. B **390**, 298 (1997).
34. A. V. Bogdan et al., Report of Budker INP №2005-33, Novosibirsk (2005).
35. J. Schwinger, *Particles, Sources and Fields*, Vol. II, Addison-Wesley Publishing Company Advanced Book Program Reading, Massachusetts (1973); M. Deers and K. Hikasa, Phys. Lett. B **252**, 127 (1990); K. Melnikov, Int. J. Mod. Phys. A **16**, 4591 (2001); A. Hofer, J. Gluza, and F. Jegerlehner, Eur. Phys. J. C **24**, 51 (2002).
36. M. N. Achasov et al., Phys. Lett. B **559**, 171 (2003).
37. N. N. Achasov, A. A. Kozhevnikov, and G. N. Shestakov, Phys. Lett. B **50**, 448 (1974); N. N. Achasov, N. M. Budnev, A. A. Kozhevnikov, and G. N. Shestakov, Yad. Fiz. **23**, 610 (1976); N. N. Achasov and G. N. Shestakov, Fiz. Elem. Chastits. At. Yadra **9**, 48 (1978).
38. N. N. Achasov and A. A. Kozhevnikov, Yad. Fiz. **55**, 809 (1992); Int. J. Mod. Phys. A **7**, 4825 (1992).
39. D. Bisello et al., Phys. Lett. B **220**, 321 (1989).
40. E. Braaten, S. Narison, and A. Pich, Nucl. Phys. B **373**, 581 (1992).
41. A. Aloisio et al., Phys. Lett. B **561**, 55 (2003).
42. S. Eidelman et al., Phys. Lett. B **592**, 1 (2004).
43. P. Estabrooks and A. D. Martin, Nucl. Phys. B **79**, 301 (1974).
44. S. D. Protopopescu et al., Phys. Rev. D **7**, 1279 (1972).
45. M. Davier et al., Eur. Phys. J. C **27**, 497 (2003); M. Davier et al., Eur. Phys. J. C **31**, 503 (2003).
46. N. N. Achasov and A. V. Kiselev, Pisma Zh. Eksp. Teor. Fiz. **75**, 643 (2002).